

Doppler Imaging of the Hertzsprung gap star OU Andromedae

Ana Borisova¹, Uwe Wolter², Renada Konstantinova-Antova¹
and K. P. Schröder³

¹ Institute of Astronomy and NAO, Bulgarian Academy of Sciences, BG-1784, Sofia,
Bulgaria aborisova@astro.bas.bg, renada@astro.bas.bg

² Hamburger Sternwarte, Gojenbergsweg 112, 21029 Hamburg, Germany
st0h311@hs.uni-hamburg.de

³ Departamento Astronomia, Universidad de Guanajuato, GTO CP 36000, Mexico
(Submitted on 17.07.2018. Accepted on 04.03.2019)

Abstract. OU And (HD 223460, HR 9024) is a moderately fast-rotating early G-type giant star, located in the Hertzsprung gap; potentially it was an Ap-star during its main sequence phase. Our data intermittently cover the years 2008 to 2017 with a few single spectra and four observing campaigns, each lasting several weeks. Using high-resolution spectra from two sites (NARVAL and TIGRE), we create photospheric Doppler images (DI) and, furthermore, analyze the evolution of OU And's chromospheric emission. We compare our DI to simultaneous Zeeman DI (ZDI) from an earlier study and include a detailed discussion of fundamental Doppler imaging limitations. During all our observations OU And has shown only feeble surface features apart from a pronounced polar spot, which is thus present in all DI and ZDI of OU And made so far. Furthermore, we find that in several instances weak features move, evolve or disappear during less than one stellar rotation. Combining our results with findings of earlier photometric campaigns, we summarize that the activity of OU And has changed from a few epochs of obvious rotational modulation in the 1980s and 90s to several epochs after 2002 without such modulation. We perform a systematic error analysis of the chromospheric activity indices on our densely sampled 2015 TIGRE data. Thus covering almost three stellar rotations, we find OU And's chromospheric emissions to be nearly constant down to a level of a few percent.

Key words: stars:individual: OU And -stars:late-type -stars:activiy -stars:starspots

1 Introduction

Our target OU And (HD 223460, HR 9024) is a single giant of spectral class G1 III (Gray et al. 2001) with moderate emission in the Ca II H&K lines (Cowley & Bidelman 1979, who did not quantify the emission). It exhibits X-ray emission (Gondoin 2003, Ayres 2007) and is a moderate rotator with a projected rotational velocity of $v \sin i \sim 21.5 \text{ km s}^{-1}$. Its position in the Hertzsprung-Russel diagram (HRD) is in the Hertzsprung gap with $T_{\text{eff}} \sim 5360 \text{ K}$ and $M = 2.85 M_{\odot}$ (see Table 1).

Our best estimates for the parameters of OU And are shown in Tab. 1, they are close to those collected and measured by Strassmeier et al. in 1999. The mismatch of the rotation period, $v \sin i$ and assumed stellar radius amounts to approximately 25%. While this is significant, we note that e.g. Gray et al. (2001) estimate a precision of 'approximately one-half temperature type and one-half luminosity class' for their spectral type classifications.

The photometric variability of OU And has been studied by Hopkins et al. (1985), Strassmeier & Hall (1988) and Strassmeier et al. (1999) who determined photometric periods between 22.3 ± 0.3 and 24.6 ± 0.4 days with V amplitudes ranging between 0.01 and 0.036 mag. The newest published photometric study of OU And (Strassmeier et al., 1999) is based on

data from 1996 and 1997, it yields a period of 24.2 days. We note that the corresponding light curve, by-eye, does not show a clearly pronounced periodic modulation, but instead apparently aperiodic variations up to about ± 0.03 mag. Citing Strassmeier et al. (1999): *'The period from our dataset [...] is not well defined and accordingly uncertain. We note that the minimum radius ... from $v \sin i$ and the photometric period [are] in severe disagreement with the spectral classification of G1III.'*

Our study focusses on the characterization of OU And's activity on timescales up to several years. To this end, we use the longest time series of spectroscopic observations available for OU And to date – covering the years 2008 to 2017. In particular, we study the large-scale geometry of spots in OU And's photosphere. Earlier Zeeman-Doppler imaging campaigns (ZDI) found that OU And's surface magnetic field is dominated by a simple geometry: all Doppler images of OU And created so far show a polar spot, which suggests that it is stable on timescales of at least several years. In combination with evolutionary models, this suggests that OU And has been an Ap-star during its main sequence phase (Borisova et al. 2016, BEAL16 in the following).

In Section 2 we describe the observations and reduction of all data presented in this paper. While section 3 describes the construction and general limitations of Doppler images (DI), Section 4 contains our analysis of the chromospheric emission. Finally, Section 5 contains our main discussion and summary. This includes a detailed comparison of our DI results with those contained in the ZDI of BEAL16.

Table 1. Fundamental parameters of OU And. The exact rotation period is still under debate, see Sec. 1 for details. The uncertainty of the inclination is not reported by BEAL16, we expect it to be about ± 10 deg.

| Parameter | Value | Reference |
|-------------------------------------|-----------------------|--|
| V , mag | 5.86 | Hipparcos catalogue, ESA, 1997 |
| Distance, pc | $129.7_{-5.5}^{+6.0}$ | van Leeuwen 2007 |
| Spectral type | G1 III | Gray et al. 2001 |
| T_{eff} , K | 5360 | Borisova et al. 2016 (BEAL16) |
| L_x , 10^{27} erg/s | 8203 | Gondoin 1999 |
| Radius, R_{\odot} | 9.46 | BEAL16 |
| Mass, M_{\odot} | 2.85 | BEAL16 |
| Luminosity, L_{\odot} | 71.2 | BEAL16 |
| $\log g$ | 2.8 | BEAL16 |
| [Fe/H] | -0.07 | BEAL16 |
| $v \sin i$, km s^{-1} | 21.5 ± 2.1 | de Medeiros & Mayor 1999 Glebocki et al. 2000 |
| P_{rot} , days | 24.2 | Strassmeier et al. 1999 |
| Inclination, deg | 45 | BEAL16 |
| Radial velocity, km s^{-1} | -2.47 | de Medeiros & Mayor 1999 |

2 Observations and Data processing

2.1 NARVAL data: Observations and reduction of spectra

Observations were carried out with the NARVAL spectropolarimeter mounted on the 2 m Bernard Lyot Telescope at Pic du Midi Observatory, France. OU And was observed during the second semesters of 2008, 2013 and the first in 2015: six observations were obtained in September 2008, 13 observations in September and October 2013, and 14 observations in the period June to August 2015. The total exposure time for each observation was 40 minutes with the exception of the first two observations : on 14 September 2008 it was 4 minutes and on 16 September 2008 it was 16 minutes. A summary is presented in Table 2. Observational data obtained in 2013 and 2015 were collected during three stellar rotations, here we could obtain a reasonably dense phase coverage.

NARVAL is a twin of the ESPaDOnS spectropolarimeter (Donati et al., 2006), it consists of a polarimetric unit connected by optical fibers to a cross-dispersed echelle spectrometer. The instrument has a spectral resolution of $R = \lambda/\Delta\lambda \simeq 65000$ and covers wavelengths from about 3690 to 10480 Å, see BEAL16 for further details.

We used the Libre ESPrIT software (Donati et al., 1997) for automatic spectra extraction and reduction, this includes wavelength calibration, heliocentric frame correction and continuum normalization. After data reduction, the extracted spectra are recorded in ASCII files; they consist of the normalized Stokes I (I/I_c) and Stokes V (V/I_c) intensities and the Stokes V uncertainty, σ_v , as a function of wavelength. Here I_c represents the continuum level. A least-squares deconvolution method (sLSD) was applied to all spectra to extract mean Stokes V photospheric profiles, see Sec. 3.1 for details. The normalized Stokes I component represents normal, non-polarized spectra, we used their sLSD line profiles for our Doppler images presented here.

2.2 The TIGRE spectra and data reduction

TIGRE is a 1.2 meter robotic telescope located at La Luz observatory, near Guanajuato in central Mexico. TIGRE is equipped with the high resolution echelle spectrograph HEROS which covers the wavelength range from 3760 Å to 8800 Å with a spectral resolution of typically 20000. HEROS has two independent optical 'arms' with a 40 Å-wide gap near 5750 Å between their respective wavelength ranges.

We obtained 121 spectra of OU And using TIGRE/HEROS from 2014 Nov 14 to 2017 Sep 20, usually taking a few spectra per year, see Table 3. In addition, we performed one densely sampled campaign that covered nearly 3 stellar rotations during 14 observing nights from 2017 Sep 2 to 2017 Nov 14. During this campaign, we normally took 10 consecutive spectra with an exposure time of 120 s each, covering about half an hour in total. The 120 sec spectra have typical signal-to-noise-ratios (SNR) of 30 at 4000 Å, 100 near the H α line and 60 in the region of the Ca IR triplet. For a few nights these consecutive observations were interrupted due to poor weather, they can be recognized by exposure times differing from 120 sec:

Table 2. Spectropolarimetric observations of OU And using NARVAL in 2008, 2013 and 2015. The corresponding activity indices for 2008 and 2013 are taken from Table 2 of BEAL16. Following BEAL16, we use $HJD_0 = 2454101.5$ and a rotational period of $24^d.2$ for ephemeris computations.

| Date | HJD 2450 000 + | Phase | S-index | H α index | Ca IRT index |
|--------------|-------------------|---------|---------|---------------------|-----------------|
| 14 Sep. 2008 | 4724.46 | 25.742 | 0.492 | 0.3338 | 0.873 |
| 16 Sep. 2008 | 4726.52 | 25.827 | 0.469 | 0.3183 | 0.856 |
| 19 Sep. 2008 | 4729.57 | 25.953 | 0.498 | 0.3391 | 0.869 |
| 21 Sep. 2008 | 4731.41 | 26.029 | 0.515 | 0.3499 | 0.878 |
| 25 Sep. 2008 | 4735.43 | 26.195 | 0.517 | 0.3421 | 0.879 |
| 29 Sep. 2008 | 4739.52 | 26.364 | 0.515 | 0.3434 | 0.870 |
| 02 Sep. 2013 | 6538.57 | 100.705 | 0.525 | 0.3366 | 0.887 |
| 08 Sep. 2013 | 6544.52 | 100.951 | 0.483 | 0.3269 | 0.864 |
| 10 Sep. 2013 | 6546.50 | 101.033 | 0.504 | 0.3335 | 0.870 |
| 15 Sep. 2013 | 6551.54 | 101.241 | 0.496 | 0.3422 | 0.866 |
| 17 Sep. 2013 | 6553.52 | 101.323 | 0.521 | 0.3515 | 0.887 |
| 19 Sep. 2013 | 6555.51 | 101.405 | 0.494 | 0.3395 | 0.874 |
| 21 Sep. 2013 | 6557.50 | 101.488 | 0.496 | 0.3397 | 0.876 |
| 23 Sep. 2013 | 6559.49 | 101.570 | 0.484 | 0.3322 | 0.873 |
| 06 Oct. 2013 | 6572.47 | 102.106 | 0.473 | 0.3357 | 0.868 |
| 08 Oct. 2013 | 6574.46 | 102.188 | 0.484 | 0.3652 | 0.854 |
| 11 Oct. 2013 | 6577.57 | 102.317 | 0.482 | 0.3421 | 0.862 |
| 13 Oct. 2013 | 6579.57 | 102.400 | 0.485 | 0.3595 | 0.866 |
| 31 Oct. 2013 | 6597.38 | 103.136 | 0.534 | 0.3466 | 0.887 |
| 26 Jun. 2015 | 7200.62 | 128.063 | 0.426 | 0.3156 | 0.827 |
| 28 Jun. 2015 | 7202.58 | 128.144 | 0.431 | 0.3277 | 0.831 |
| 30 Jun. 2015 | 7204.60 | 128.227 | 0.443 | 0.3222 | 0.841 |
| 06 Jul. 2015 | 7210.62 | 128.476 | 0.480 | 0.3415 | 0.872 |
| 08 Jul. 2015 | 7212.63 | 128.559 | 0.485 | 0.3383 | 0.875 |
| 10 Jul. 2015 | 7214.61 | 128.641 | 0.518 | 0.3425 | 0.873 |
| 12 Jul. 2015 | 7216.59 | 128.723 | 0.474 | 0.3182 | 0.860 |
| 14 Jul. 2015 | 7218.60 | 128.806 | 0.433 | 0.3131 | 0.837 |
| 20 Jul. 2015 | 7224.58 | 129.053 | 0.467 | 0.3268 | 0.848 |
| 06 Aug. 2015 | 7241.66 | 129.759 | 0.474 | 0.3249 | 0.858 |
| 10 Aug. 2015 | 7245.61 | 129.922 | 0.442 | 0.3111 | 0.848 |
| 18 Aug. 2015 | 7253.52 | 130.249 | 0.507 | 0.3392 | 0.872 |
| 25 Aug. 2015 | 7260.53 | 130.538 | 0.485 | 0.3439 | 0.870 |
| 28 Aug. 2015 | 7263.66 | 130.668 | 0.464 | 0.3295 | 0.856 |

either the TIGRE system had to abort an exposure or it prolonged an exposure to compensate for poor seeing or sky transmission. As discussed in Section 4.3, we used the 10-shots-per-night sampling to reliably estimate the uncertainties of the measured chromospheric line fluxes for each night.

We reduced the TIGRE spectra using version 'v3' of the TIGRE/HEROS pipeline (Mittag et al., 2018), based on the REDUCE package and written in IDL (Piskunov & Valenti, 2002). The pipeline follows the usual steps of reducing echelle CCD frames. The TIGRE pipeline does not make use of the 2-dimensional flatfield processing of REDUCE. Instead, it extracts the flatfield information along the orders into '1D-flatfields', using the same procedure and parameters as the subsequent extraction of the science spectra.

The pipeline uses ThAr exposures of the same night as each target

Table 3. TIGRE spectra of OU And taken 2014, 2015 and 2017, exposure times are given in seconds. For densely sampled time series, all spectra were taken consecutively with the given exposure time during less than one hour, their number is given in brackets; here the JD represents the start of the first spectrum of each series. The JD offset is the same as in Figs. 7 to 9, phases are computed with the same ephemerides as given in Tab. 2.

| Date | exp.time | JD-2456976.0 | Phase |
|-------------------|----------|--------------|---------|
| 14 Nov. 2014 | 1080 | 0.594 | 118.806 |
| 10 Jul. 2015 | 360 | 238.944 | 128.655 |
| 12 Jul. 2015 | 1095 | 240.955 | 128.738 |
| 02 Sep. 2015 | 181 | 275.867 | 130.180 |
| 06 Sep. 2015 (10) | 120 | 296.758 | 131.044 |
| 21 Sep. 2015 (10) | 120 | 311.755 | 131.663 |
| 25 Sep. 2015 (4) | 120 | 315.737 | 131.828 |
| 26 Sep. 2015 (10) | 120 | 316.700 | 131.868 |
| 01 Oct. 2015 (10) | 120 | 321.706 | 132.075 |
| 13 Oct. 2015 (10) | 120 | 333.756 | 132.573 |
| 14 Oct. 2015 | 100 | 334.696 | 132.611 |
| 15 Oct. 2015 | 115 | 335.601 | 132.649 |
| 19 Oct. 2015 (10) | 120 | 339.676 | 132.817 |
| 25 Oct. 2015 (10) | 120 | 345.659 | 133.064 |
| 04 Nov. 2015 (10) | 120 | 355.582 | 133.474 |
| 10 Nov. 2015 (10) | 120 | 361.610 | 133.724 |
| 14 Nov. 2015 (10) | 120 | 365.661 | 133.891 |
| 04 Jun. 2017 | 180 | 933.958 | 157.374 |
| 19 Jun. 2017 | 180 | 948.947 | 157.994 |
| 30 Jul. 2017 | 240 | 989.881 | 159.685 |
| 20 Sep. 2017 | 373 | 1041.732 | 161.828 |

spectrum to perform a wavelength calibration. In order to average over temperature and other changes affecting HEROS, it computes an average ThAr frame by combining exposures from the beginning and end of each night.

2.3 The TIGRE/HEROS activity indices

As a final step, the TIGRE pipeline computes line core indices to measure the core flux for the combined CaII H&K lines, called S_{TIGRE} in the following. Furthermore, line fluxes are determined individually for the three CaII IR lines ($S_{IRT-8498}$, $S_{IRT-8542}$ and $S_{IRT-8662}$). The computation of the S_{TIGRE} indices is analogous to the computation of the Mt. Wilson S-index: after a radial velocity correction using a synthetic template spectrum, it sums up the spectral counts of two 1Å-wide intervals centered on the CaII H&K line cores. Finally, it divides by the integrated counts of two nearby 20 Å-wide reference intervals, see Fig. 1 of Mittag et al. (2016) for details. In contrast to the original Mt. Wilson index, S_{TIGRE} uses a box-car weighting instead of a triangular weighting function, centered on the emission line cores. The S_{IRT} indices also use 1Å-wide intervals centered on each line, as well as reference intervals of different widths between 2 and 10 Å, see Fig. 1 of Mittag et al. (2017) for the detailed definitions.

Currently, the TIGRE pipeline does not compute the S_{TIGRE} index for spectra whose mean SNR in the blue arm falls below a somewhat arbitrary threshold of 15. Due to this threshold, we lose about 30 index measurements. Anyway, we restrict our analysis to activity indices computed by the pipeline and independently estimate their uncertainties, see Sec. 4.3 for details.

3 Doppler imaging of the NARVAL spectra

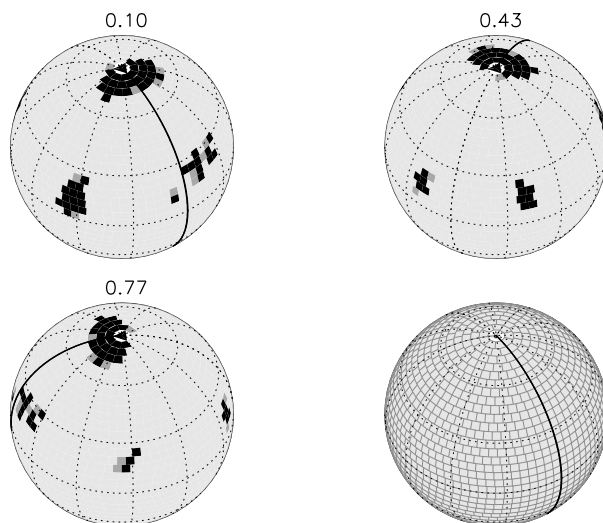


Fig. 1. Photospheric Doppler image (DI) of OU And computed from our 2008 NARVAL spectra, using our DI package CLDI. All maps show the same surface for the indicated rotation phase; the sub-observer longitude at phase zero is marked by a thick line. The fourth map shows the empty surface grid used for our DI, it has 2048 elements, each extending by 4.5×4.5 square degrees. Black and gray elements indicate a spot filling factor of 100% and 50%, respectively.

3.1 Least squares deconvolution: sLSD

To obtain spectral line profiles from the unpolarized (Stokes I) component of our NARVAL spectra, we use our least-squares deconvolution method, called “selective least-squares-deconvolution” (sLSD, see Wolter et al. 2005). sLSD computes an average broadening profile for the lines in one or several narrow spectral regions, each typically a few 10 \AA wide. Like other LSD algorithms, it deconvolves a rotationally broadened spectrum using a narrow-lined spectrum as a template (see eg. Barnes et al. 2000 and references there).

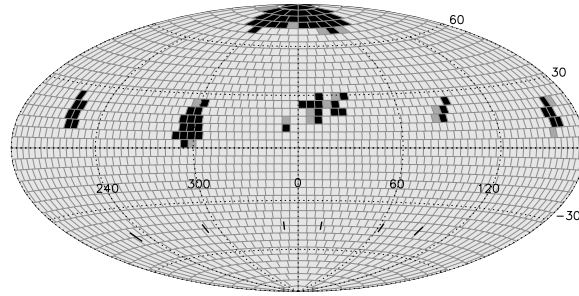


Fig. 2. Aitoff projection of *the same DI* as that shown in Fig. 1 – i.e. reconstructed from our 2008 NARVAL spectra. The sub-observer longitude at phase zero is the meridian at the centre, marked by zero. Rotation phases sampled with spectra are indicated by the marks on the southern hemisphere, only six for this year. Rotation progresses with *decreasing* surface longitude, i.e. from left to right in this projection.

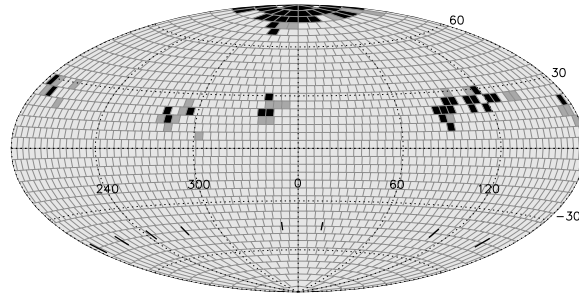


Fig. 3. Same as Fig. 2 for the DI computed from our 2013 NARVAL spectra.

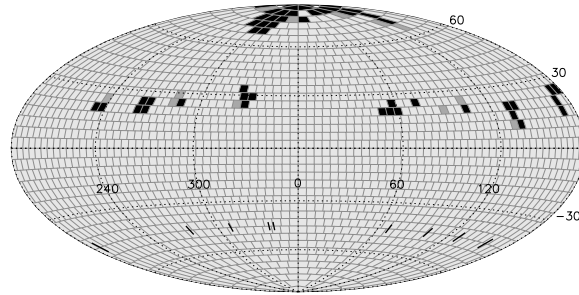


Fig. 4. Same as Fig. 2 for the DI based on our 2015 NARVAL spectra. The line profiles analyzed for this image are shown in Fig. 5. As discussed in Section 3.3, we did not use the 2015 August spectra as input to the CLDI, because intrinsic spot evolution during less than one rotation inhibited the construction of a DI.

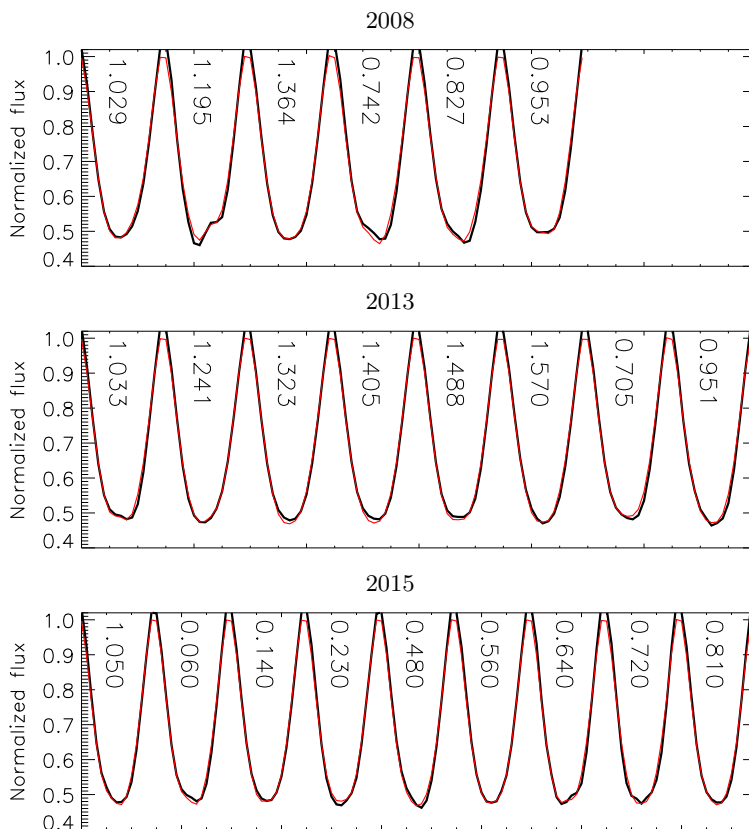


Fig. 5. Least-squares deconvolved (sLSD) line profiles for 2008 (top panel), 2013 (middle) and 2015 (bottom). They were computed from our NARVAL Stokes I spectra (i.e. the non-polarized signal) and used as input for our Doppler images. The sLSD profiles are shown in black, the CLDI fits are plotted red. Rotation phases are annotated for each profile, including a leading rotation number to show the actual order of the corresponding observing dates.

Here we use a PHOENIX synthetic spectrum in the spectral range around 6440 \AA as a template, see e.g. Husser et al. 2013. This spectrum was computed from a 1D model atmosphere with an effective temperature of 5700 K and a $\log(g)$ of 3.0 ; we downloaded it from the model library of Husser et al. (2013), further details are described there. We chose these two parameters in accordance with those used for ZDI in BEAL16 – and note that they do not closely match the stellar parameters given in Table 1. However, we have checked that variations of up to 300 K in effective temperature and ± 0.5 in $\log(g)$ do not significantly affect the resulting sLSD profiles for our spectra of OU And. We have compared our sLSD-deconvolved line profiles of OU And with those supplied by the NARVAL pipeline (based on a LSD implementation described e.g. in Donati et al., 1997). The sLSD and

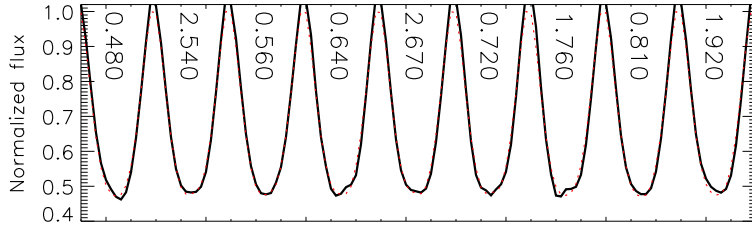


Fig. 6. Same as Fig. 5, showing the end of our complete sLSD profile time series of 2015. This includes those phases $\phi \geq 1.76$ that we did not use for the CLDI Doppler image, because of significant spot reconfigurations after the first sampled rotation (phase interval 0.06 to 1.05, see Fig. 5). Essentially this means, that the star changes appearance during one Doppler imaging ‘exposure’. The resulting poor fit of the CLDI line profiles (red) to their observed counterpart (black) is clearly visible at phases 0.64, 1.76 and, less pronounced, at 1.92. See Sec. 3.3 for discussion.

LSD profiles agree well, apart from minor differences in the quasi continuum surrounding the line. However, we used the sLSD profiles because they are slightly easier to use in the framework of our Doppler imaging package CLDI, which we describe in the following section.

3.2 Photospheric Doppler imaging: CLDI

For each rotation phase observed with NARVAL, application of sLSD yields one line profile (strictly speaking a rotational-broadening-function, RBF) that averages the rotational broadening of the lines in the spectral region input to sLSD. More precisely, when convolving this RBF with the template spectrum and multiplying it with a low-order polynomial, it will reproduce the observed spectrum within the limits of the noise of the spectra. The polynomial is used to adapt the quasicontinua of the template and observed spectrum (see Wolter et al. 2005 for details). As a final preparatory step, we apply a simple fitting routine to determine the linear limb-darkening coefficient of the RBF. For all our NARVAL datasets, this yielded a value of 0.7. Then, the above parameters, all line profiles and all corresponding values of rotation phase are passed to the CLDI algorithm.

The Doppler images of OU And were constructed with the same values of $v \sin(i) = 20.5 \text{ km.s}^{-1}$, $i = 45^\circ$, $P_{rot} = 24.2 \text{ d}$ as those used for the ZDI imaging of BEAL16. We attempted to independently estimate the P_{rot} and stellar inclination on the basis of the goodness of the line profile fit. Unfortunately, given the overall – at best – moderate rotation phase coverage of our spectra and – at times – fast spot evolution (compared to the rotation period) the CLDI tomography of our NARVAL data does not allow to determine the rotation period at all. Concerning the inclination of the stellar rotation axis, we can exclude large inclinations exceeding ≈ 60 degrees and find that the CLDI favours lower inclinations of about 45 degrees or less. This is in agreement with the inclination given in Table 1, i.e. the value determined by BEAL16 during the ZDI process. Presumably,

in this case, ZDI is more powerful in determining the stellar inclination for two reasons: (i) it combines the information of more than one Stokes component (two in the case of BEAL16). Furthermore, (ii) the magnetic features in OU And’s atmosphere may be more coherent than their cool-spot counterparts. Comparing our DIs presented here and BEAL16’s ZDI suggests such a different coherence, see Section 5.2.

We assume rigid rotation for the DI, i.e. no differential rotation that significantly affects our reconstruction. We note that a relatively fast rotating giant star like OU And may exhibit significant surface differential rotation up to several percent in terms of $\alpha = \Delta\Omega/\Delta\Omega_{eq}$ (Kóvari et al. 2017). Early on during our analysis we tentatively tried several DI reconstructions of OU And which included a non-zero differential rotation with a solar-like \sin^2 law for the angular velocity as a function of latitude. However, we did not find an improved convergence of our DI for any reasonable value of α . Thus, based on our data, we cannot determine the differential rotation of OU And. However, our line profile time series finally used for DI only span up to one stellar rotation, see Fig. 5. In this case, even a tentative differential rotation of OU And with up to $\alpha \approx 0.1$, in agreement with the values of Kóvari et al., would not strongly affect our images.

We used the same internal settings of CLDI as described and used in Wolter et al. 2008. For all three NARVAL spectral time series (2008, 2013 and 2015), CLDI stopped to converge after 30 to 40 iterations. As discussed in Sec. 3.4, it may turn out at this step that, inside the time series used for DI, some line profile deformations do not periodically re-appear after an integer number of rotations. Such cases always lead to a poor convergence of CLDI. As a result, the observed line profiles are fitted poorly in the sense that these ‘non-periodic’ line profile deformations are largely not fitted at all. A closer look at the line profiles in Fig. 6 around phases 0.7, 1.7 and 2.7 is instructive here. As an example, we compare the line profiles at phases 0.72 and 1.76: while the relatively weak deformations of the OU And profile at 0.72 are largely fit by the CLDI model, this is not the case for phase 1.76. Yet, these two profiles sample close rotational orientations of the star, only $0.04 \cdot 360^\circ = 15$ degrees apart – plus one full rotation that is ‘assumed’ to make no difference in spot distribution by CLDI. If the spot distribution on OU And had not changed during this complete rotation, the two line profiles in our example would essentially look the same.

We then step-by-step reduced the phase range of the DI input time series, i.e. we removed the corresponding line profiles from the CLDI input data. As discussed in the following section, this turned out to be necessary only for the 2013 and 2015 data. In both cases, this indicates that, during our observations, several spots substantially changed their size and position during less than one rotation. We note that this does not hold true for the polar spot, since such a spot dominantly creates a constant (i.e. not rotationally modulated) deformation at the line profile center.

3.3 Rotation phase intervals not used for CLDI

Given the short overall duration of the 2008 NARVAL time series and the large phase gap before phase 0.742 (see Fig. 5), we could make use of all

available spectra to build a DI. However, in spite of comparatively pronounced profile deformations (e.g. at phase 1.195), our sparse phase coverage in 2008 only yields approximate information about the spot distribution on OU And.

In the 2013 time series, the profile deformations appear somewhat weaker, but the observing campaign covered more than one rotation of OU And. As described above for the 2015 time series, we step-by-step removed input spectra from the time series used for CLDI, finally ending up with only using the September 2013 spectra. We note that, even with this restriction, the profiles around phase 1.405 exhibit a slight mismatch of the observed and modelled line profiles, see Fig. 5. While this presumably indicates a short-lived reconfiguration of a spot(group) around that phase, we cannot constrain this any further on the basis of our observations.

Our 2015 observations offer the longest time series, they cover almost three rotations with 14 spectra, albeit with a rather uneven sampling. As Fig. 6 illustrates, CLDI converges poorly when working on the whole time series; several pronounced profile deformations are not fitted at all – e.g. at phases 0.64 and 1.76. Because the time series is most densely sampled at its beginning, we successively removed observed phases at its end from the time series of spectra. After removing six such phases, the time series covers quite precisely one rotation and CLDI finally yields a proper fit to the observed profiles, as illustrated in Fig. 5.

3.4 Resolution and caveats concerning (not only) our DI

When a star rotates sufficiently fast, in terms of $v \sin(i)$, its line profiles contain a one-dimensional projection of surface inhomogeneities on the visible stellar disk at each phase. This is the basis of the Doppler imaging technique (DI) as used by A. Deutsch and others already in the 1950s (e.g. Deutsch 1958). DI uses a time series of such line profiles to reconstruct surface features, usually starspots or abundance variations, in the stellar atmosphere. To achieve significant surface resolutions, DI requires low-noise, densely sampled time series of high resolution stellar spectra, see Strassmeier et al. (2009) for an overview.

We use our implementation of the method, called Clean-like Doppler imaging (CLDI, see Wolter et al. 2005) to reconstruct starspots on OU And’s surface, i.e. cooler regions in its photosphere. Similar to the image deconvolution method CLEAN used in radio astronomy (Högbom 1974) it performs an iterative reconstruction of the stellar surface, building up an increasingly good model of the observed line profiles. Given suitable spectral data, the method can be extended to the chromosphere, see Wolter et al. (2008) – unfortunately, the phase sampling of our OU And spectra did not allow such an analysis.

When interpreting our CLDI results, it is important to keep the caveats in mind that apply to all Doppler images (see e.g. Wolter et al. 2005 as well as Khochukhov & Piskunov 2002 and references there):

(i) every DI is based on a time series of 1-dimensional projections along the stellar rotation axis. This fact limits the latitude resolution of DI, especially for unevenly time-sampled data or a poorly known stellar inclination i . Roughly speaking, to resolve surface features with a resolution of

e.g. 10 degrees on the stellar surface, one needs a sufficiently dense phase sampling of at least about 36 spectra evenly sampling a complete rotation.

Furthermore (ii), the spectral resolution and non-rotational line broadening mechanisms limit the achievable resolution of DIs: Again as a rule-of-thumb, aiming e.g. for a 10 degree resolution on the stellar surface, the analyzed spectra need to resolve $\approx 10/180 \approx 5\%$ of the entire line profile. As an example, for a star with $v \sin(i) = 100 \text{ km/s}$ the spectra would need to resolve $\approx 0.05 \cdot 200 \text{ km/s} = 10 \text{ km/s}$, translating into a spectral resolution of 30000. Additionally, the intrinsic line broadening mechanisms must not significantly exceed that value. Applying this estimate to our NARVAL data of OU And, the spectral resolution of 65000 translates into a velocity resolution of $300000/65000 \text{ km/s} \approx 4.5 \text{ km/s}$ which resolves the typical overall width of OU And's line profiles of $2 \cdot v \sin(i) = 43 \text{ km/s}$ with close to 10 resolution elements. This translates into an approximate upper limit of $180/10 \approx 20$ degrees for the surface resolution of our DI. While this is a meaningful *lower limit* to their resolution in surface latitude and longitude, this approximate resolution can at best be achieved for time intervals with a correspondingly dense phase sampling, see item (i) above.

As a further caveat (iii), a wrongly assumed stellar inclination, by e.g. 20° or more, will significantly distort the resulting DI. According to our experience, Doppler imaging can be used to determine stellar inclinations up to a precision of $\approx 10^\circ$ in some cases (see e.g. Wolter et al. 2005). However, this requires evenly phase-sampled spectra of a star showing well-defined and resolved periodic deformations in its line profiles. This is not the case for our OU And spectra. However, the situation is more favourable for the corresponding Zeeman Doppler images (ZDI = 'magnetic' DI) based on the same spectra, see BEAL16, because the Stokes V profiles show coherent and somewhat pronounced deformations. Therefore we use the stellar inclination of 45° determined there. Yet, it should be kept in mind that this value comes with an incompletely known uncertainty.

An obvious caveat (iv) is that the noise level of the input line profiles needs to be sufficiently low to resolve the relevant surface-induced line deformations. Apart from adequately well exposed spectra, least-squares deconvolution methods (LSD) are often used to reduce the noise by combining the profile information of several or even very many lines. Here, we use our sLSD algorithm described above.

Also, obviously (v), when combining observations obtained during more than one rotation, the spot features need to survive sufficiently long. Faster changing features will in many cases lead to poorly converging DI iterations, the same may apply for a wrongly assumed differential or rigid rotation. In other cases such fast changes may lead to massive and unnoticed image artifacts when accompanied by a poor phase sampling. This aspect is discussed in Sections 3.2 and 3.3 above with regard to our Doppler images of OU And.

Finally (vi), for unevenly sampled phase intervals, in particular phase gaps in the observations, the latitude information in the resulting DI can be severely warped in parts of the reconstructed surface. Given the uneven phase sampling during *some time intervals* of our spectral time series, this caveat needs to be kept in mind. In the presence of poorly defined latitude information, many DI algorithms, including CLDI, tend to place surface

features close to the sub-observer latitude – see Wolter et al. (2005) for a detailed discussion. As a sidenote, it is a little surprising, that the mid-latitude features of our DI of OU And concentrate at latitudes close to 30 degrees (while the sub-observer latitude is 45 degrees). However, we did not analyze this any further.

To conclude our discussion of Doppler imaging caveats, we note that we consider the polar spot, found in all our DIs of OU And, to be real. This means we are certain that it is not an imaging or line profile modeling artifact. See e.g. Bruls, Solanki & Schüssler (1998) for a detailed discussion of this aspect. Yet, the shape and size of the polar spot shown in our DI maps are only poorly defined, given the relatively small $v \sin(i)$, the potential uncertainties in stellar inclination, the partially uneven phase sampling and, may be, most importantly, the rather weak line profile deformations in our spectra of OU And.

4 Chromospheric emission

4.1 Overview of all data from 2008 to 2015

BEAL16’s figures 1 and 6 show their H_α -, S- and Ca IRT-indices measured in the 2008 and 2013 NARVAL spectra. The variations of all chromospheric line indices in those data were relatively weak, little more than 10% peak-to-peak in the H_α - and S-indices. The phase-folded data of 2008 show one pronounced dip around phase 0.8. However, since the 2008 data only cover one contiguous rotation, it is impossible to say, based on the 2008 spectra, whether this dip is due to rotational modulation. It could, just as well, be due to a fast spot reconfiguration – the available phase sampling does not allow to determine this. In the 2013 data, with a better phase sampling, only the H_α index clearly suggests a rotational modulation, while the S- and Ca IRT-indices vary more erratically when comparing different rotations.

To complement and continue the analysis of BEAL16, we measured the H_α -, S- and Ca IRT-indices in our 2015 NARVAL spectra, using the same routines as they did at the time. Our measurements are given in Table 2. Furthermore, we measured chromospheric line indices in our TIGRE spectra, namely a Ca H&K index S_{TIGRE} , as well as individual indices for all three Ca IRT lines. For these measurements, we used the line indices supplied by the TIGRE pipeline. It should be kept in mind that the TIGRE line indices cannot be directly compared to their NARVAL counterparts, mostly because the spectral resolution of TIGRE only amounts to about one third of NARVAL’s. This makes the TIGRE activity indices significantly less sensitive to chromospheric emission variations than the NARVAL measurements.

We show the NARVAL S-index measurements and their TIGRE counterpart in Figure 7. For the conversion of the S_{TIGRE} index to Mt. Wilson S-index values, we used Eq. (2) of Mittag et al. 2016. Strictly speaking, this conversion has only been calibrated for dwarf stars. However, for luminosity classes IV and III, the same calibration can also approximately be used (priv. comm. M. Mittag).

With all the above caveats in mind, the combined measurements of Fig. 7 allow the following statements: during the nearly three years covered

by the combined TIGRE and NARVAL 2015 data, OU And has not shown any variations in chromospheric flux strongly exceeding those observed in 2008 and 2013. A small exception occurred during one night of TIGRE observations where the S-index exceeds a value of about 0.55, clearly visible in Fig. 9 near day 360. Furthermore, the lowest NARVAL S-indices in 2015 reach down to about 0.43 – approximately 10% lower than the lowest S-indices measured by BEAL16 for 2008 and 2013.

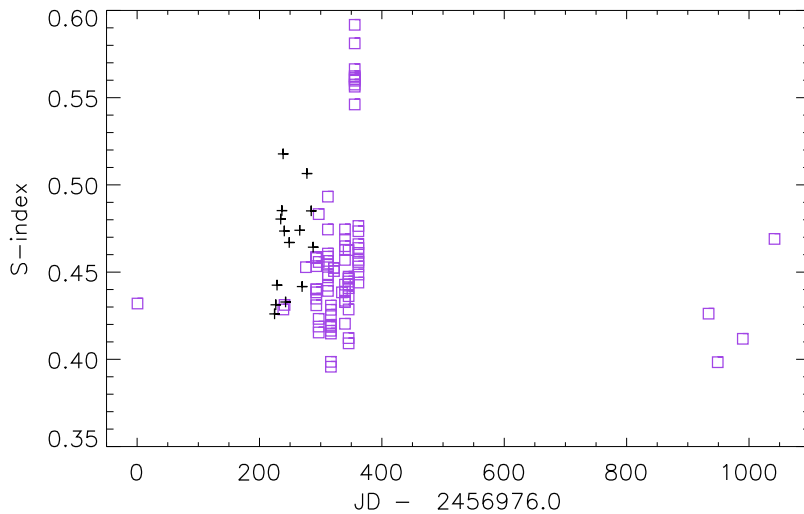


Fig. 7. S-indices for all our TIGRE spectra (squares, 2014 Nov 14 to 2017 Nov 14) and S-indices measured in our 2015 NARVAL spectra (plus symbols). The JD is given relative to the date of the first TIGRE observation. See Fig. 9 for a detailed analysis of the densely sampled time interval around day 350.

4.2 Chromospheric fluxes in the NARVAL spectra of 2015

All NARVAL chromospheric line indices of 2015 are shown in Fig. 8. For normalization, the time series of each index has been divided by its mean. Comparing the evolution of the three indices shows that they all show 'synchronous' variations. Whether the few and small deviations from this synchronous behaviour are physical in nature or due to measurement errors is hard to tell given the rather small number of values. As expected, the S-indices show slightly more pronounced variations than their $H\alpha$ and Ca IRT counterparts. The variations amount to 20% peak-to-peak.

While these variations are most certainly attributable to the star, phase-folding the 2015 NARVAL chromospheric measurements does not reveal a well-defined rotational modulation. Thus, our relatively sparse phase

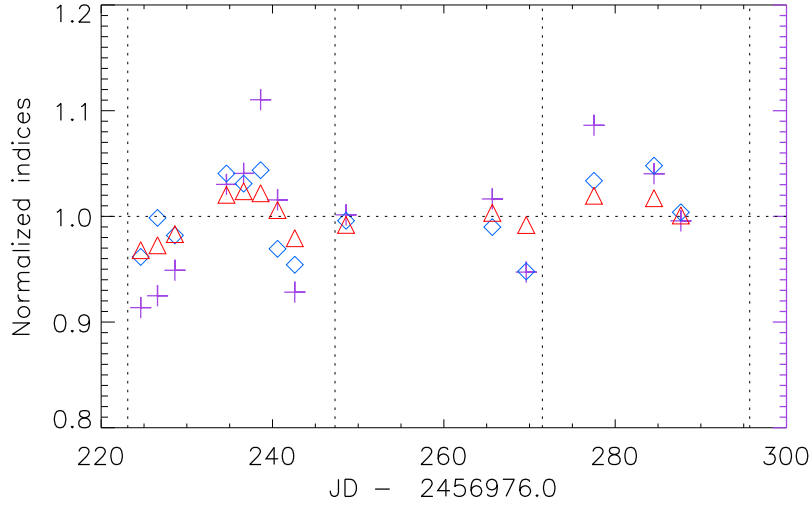


Fig. 8. All activity indices measured in our 2015 NARVAL spectra, each time series is normalized to its mean value. Crosses represent the Ca H&K S-index, diamonds and triangles the H α and Ca IRT indices, respectively. Individual measurements are given in Table 2; vertical lines mark rotation phases zero, using the period and ephemeris given there.

sampling after about day 245, combined with the intrinsic (meaning non-periodic) variations of OU And inhibit a significant detection of a periodic modulation. Nevertheless, during all three rotations marked in Fig. 8, the chromospheric emission appears to follow the modulation suggested by the values before day 245.

4.3 Analysis of the TIGRE spectra 2014 – 2017

As explained above, the chromospheric indices measured in the TIGRE spectra are less sensitive than those from the NARVAL spectra. Furthermore, the current version of the TIGRE pipeline only performs an incomplete removal of cosmic ray hits on the CCD, which causes occasional 'outliers' in the time series of TIGRE indices. To obtain reliable error estimates for the TIGRE indices, also dealing with outliers in a robust way, we used the following procedure.

As illustrated by Fig. 7 and discussed in Sec. 2.2, our TIGRE observations of OU And in 2015 normally consisted of 10 directly consecutive spectra for each observing night. We used the ASTROLIB procedure RESISTANT_MEAN⁴ to robustly estimate, for each night, the mean and standard deviation of the TIGRE indices. We selected an outlier rejection

⁴ Available and documented at <https://idlastro.gsfc.nasa.gov>

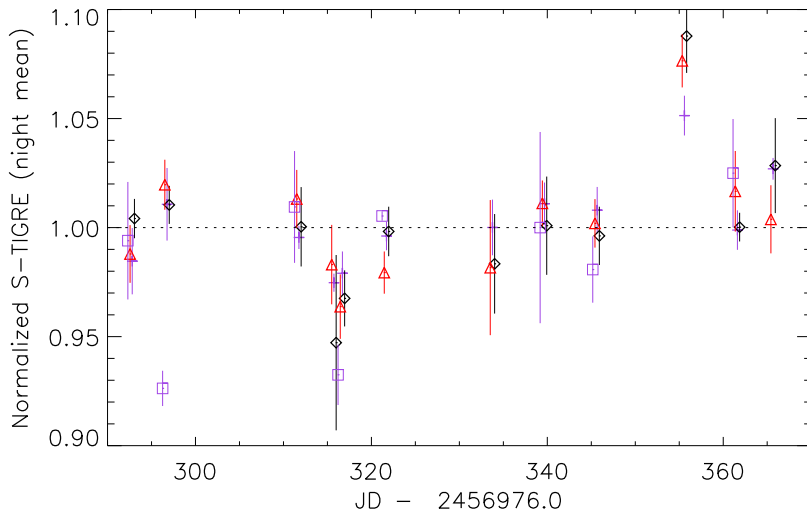


Fig. 9. Same as Fig. 7 for our densely sampled TIGRE spectra (September to November 2015). Here, we only show the *robustly estimated* mean and 1-sigma standard deviation for each night, which is computed after an outlier rejection, see Sec. 4.3 for details. All points are slightly shifted along the abscissa for each night for better visibility, the corresponding spectra were taken strictly simultaneously. Different symbols represent different lines: the S-Index is represented by violet squares; the TIGRE indices for the Ca IR are marked by blue plus symbols (8489 Å), black diamonds (8542 Å) and red triangles (8662 Å), respectively. Each line index is normalized to the median of its time series. In this way every symbol represents the mean and standard deviation of typically 8 to 10 individual measurements; the Poisson-dominated error of each measurement is, again typically, about 1 percent.

at 2.5σ , i.e. all values exceeding 2.5 standard deviations from the mean of a night were not used for the analysis. In this way, about 1/10 of the TIGRE index measurements were flagged as outliers.

The resulting, robustly estimated, chromospheric TIGRE indices are shown in Fig. 9; each time series has been divided by its mean value for a common normalization, in the same way as in Fig. 8. The error bars represent the corresponding standard deviations, computed individually for each night. The TIGRE pipeline supplies error estimates for the chromospheric indices which are based on the (in this case Poisson-dominated) noise of the integrated wavelength intervals. For almost all our spectra, these pipeline error estimates amount to a relative uncertainty close to 1 percent.

We assume in the following that the variations during each TIGRE visit, i.e. during less than one hour, are not caused by OU And itself, but are instead dominated by measurement errors. We inspected the correlation of all TIGRE indices for directly subsequent exposures of OU And during each visit. This inspection showed an uncorrelated behaviour of the different lines on these short timescales – thereby supporting the above assumption. Thus,

the error bars in Fig. 9 illustrate that the pipeline’s estimate of typically 1 percent for all individual measurements is approximately realistic – we manually checked on a few spectra that it propagates the Poisson noise of the input spectra correctly into the S_{TIGRE} index. However, for most nights, it underestimates the true measurement uncertainty by a factor of about two, only occasionally more. Again based on visual inspection of several spectra, we assume that this is mostly due to the outlier measurements discussed above.

Finally, we take another look at Fig. 9. It shows that, during the 11 nights of our 2015 TIGRE campaign of OU And, the chromospheric emission deviated significantly from the overall mean only on two nights: the dip close to day 315 and the spike near day 355. Even if the sensitivity of the TIGRE chromospheric indices is lower than that of the NARVAL indices, our TIGRE measurements again demonstrate the weak variations of OU And’s activity during most of our observations.

5 Summary

5.1 Comparing features among our CLDI maps: 2008 to 2015

Qualitatively, our three CLDI maps of OU And, shown in Figs. 1 to 4, look similar: they all (i) exhibit a polar spot hardly changing in size as well as (ii) some small mid-latitude spots slightly below 30° latitude. Those mid-latitude spots are most pronounced in the 2008 image, which corresponds to the slightly stronger line profile deformations in the 2008 time series, as compared to the data of the other two years (see Fig. 5). In particular, all profiles from 2008, except for those observed at phases 1.029 and 1.364, are markedly deformed.

In the light of the discussion of Sec. 3.4, we think that further comparison of our three DI should be limited to a few aspects. Especially comparing the longitudes of the mid-latitude spots between our three images is meaningless for two reasons. First of all, the incompletely known uncertainty of OU And’s rotation period – possibly of the order of one day, see Sec. 1 – introduces an uncertainty of the order of $1 d/24 d \cdot 360^\circ \approx 10^\circ$ in longitude for each rotation that has gone by. Given that there are 14 to 15 stellar rotations between each of our subsequent NARVAL observing runs, this results in an uncertainty of potentially up to $\approx 150^\circ$ when comparing longitudes between images about one year apart. Some uncertainty also arises due to the currently unknown differential rotation of OU And. Secondly, our 2008 and 2015 datasets used for the CLDI exhibit sampling gaps up to about 0.25 in phase. And the shape and position of DI features sampled close to these gaps are only poorly defined.

The same uncertainty may also affect the asymmetric shape of the polar spot in the 2008 image: the spot is limited to longitudes roughly between 300° and 60° because the observation phases are somewhat concentrated there (see the phase marks in Fig. 2). Thus, we believe that the named asymmetry is a reconstruction artefact for the DI of 2008. On the other hand, the asymmetry of the polar spot in the 2015 image seems to be much better supported by the denser and more homogeneous phase sampling. Thus, the spot during our 2008 observing epoch may well be asymmetric

too – but we cannot reliably determine that, based on our sparse phase sampling in 2008.

Nevertheless, given the ubiquitous deformation of line profiles of OU And, we do not doubt the reality of the polar spot in our images in any way. Furthermore, even if some of our mid-latitude spots are presumably spurious, we can constrain their latitude reasonably well: since we observe the rather fast migration of several deformations through the line profiles, we can conclude that the corresponding spot features are significantly detached from the pole.

The chromospheric emission measured during our 2015 DI campaign has, during some rotation phases, been slightly weaker than observed in any spectrum of the 2008 and 2013 DI campaigns. On the other hand, the polar spot in our 2015 DI is a little less pronounced than its 2008 and 2013 counterparts. Now, as discussed above, the 2008 DI should be interpreted with care, due to its rather poor phase sampling. Nevertheless, the weaker polar spot and the simultaneously weaker chromospheric emission in 2015 could be physically related. However, we see no further option to test that hypothesis.

In summary, our photospheric Doppler images are merely three snapshots taken during seven years, i.e. during more than 100 stellar rotations. Keeping this snapshot-like nature of our observations in mind, however, the general appearance of OU And’s photosphere has remained *qualitatively* unchanged during all our observations analyzed here.

5.2 Comparison of CLDI and ZDI maps for 2008 and 2013

BEAL16 presents Zeeman Doppler images (ZDI) of OU And for 2008 and 2013, reconstructed from the same NARVAL spectra as our photospheric CLDI images. They are shown in Figures 3 and 5 of BEAL16.

We now compare those two ‘magnetic’ ZDI maps, each containing the three spatial components of OU And’s magnetic field, with their ‘dark-spot’ CLDI equivalents. The following discussion concentrates on the radial field maps of the ZDI. For the 2013 observations, the other magnetic field component maps allow the same conclusions. For the 2008 data, only the radial field ZDI map contains well defined features – essentially only one, namely the polar spot. The 2008 meridional field ZDI map only contains very weak spots which are presumably spurious. The 2008 azimuthal field map contains the extended $\approx +200G$ spot centered close to phase 0.6. However the almost complete coincidence of this large spot with the large phase gap of the observations suggests that it may, largely or to some extent, be an imaging artefact.

Thus, concentrating on BEAL16’s ZDI radial field maps of OU And, we find that their qualitative appearance is remarkably similar to our photospheric CLDI maps: The ZDI and CLDI maps are all dominated by an extended polar spot. Furthermore, as the CLDI maps do, their ZDI counterparts exhibit a few weakly defined spots at mid latitudes. As discussed in the previous section, we believe that several, maybe all, of those features are spurious. By this we mean that, given the numerous rotationally modulated line profile deformations, we are certain that there are lower-latitude spots, but their relative weakness and often sparse phase coverage does not allow to reconstruct them in detail.

To compare *longitudes* between our CLDI and the ZDI images, it is important to note that they are 'mirror images' of each other. While rotation phase increases to the right in the ZDI maps of BEAL16, the star in our CLDI maps rotates with *decreasing* longitude. This means that, in effect, rotation phase increases to the left in our CLDI maps. As a concrete example, phase 0.25 corresponds to a longitude of 270° in our maps. We note in passing that both map orientations are in use in the DI community: while e.g. Donati et al. use the same orientation as we do (see e.g. Fig. 8 of Donati et al. 1997), other authors use the orientation of BEAL16 (see e.g. Fig. 5 of Khochukhov et al. 2004, who render the visible stellar pole as the 'south' pole of their maps). As a final remark, we note that BEAL16's ZDI maps, as all Mercator projections, are not equal-area. In particular, the size of polar regions appears massively exaggerated there. While our Aitoff projected maps are fairly better in this respect, it is instructive to consult our Fig. 1 to judge the true size of the polar spots in all maps of OU And discussed here.

Only the better phase-sampled 2013 observations allow a closer comparison of features between ZDI and CLDI images. The most conspicuous property of the polar spot in the ZDI image is its extension towards the equator, centered at phase 0.1. This phase corresponds to a longitude of $(1 - 0.1) \cdot 360^\circ = 324^\circ$ in our CLDI maps – where, indeed, the polar spot in our maps shows its most prominent extension. The mid-latitude spot close to this longitude suggestively coincides with this extension, but given the rather sparse phase sampling around phase 0, its latitude is only poorly determined. Thus, this spot at about 340° longitude may actually be closer to the pole than it appears on our CLDI map.

Another pronounced feature of the 2013 ZDI radial field map is the structure around phase 0.9 which also appears as an extension of the polar spot. This extension, however, 'leaks' stronger to lower latitudes with somehow blurred features extending down to the equator in the phase range of about 0.6 to 0.9. Taking 0.75 as an average value of this phase range, this corresponds to a longitude of $(1 - 0.75) \cdot 360^\circ = 90^\circ$ where also our CLDI map shows its strongest mid-latitude spots. But, given the truly sparse phase coverage here, a further comparison of features is presumably fruitless.

5.3 What do we learn about OU And?

Strictly speaking, our CLDI Doppler images presented here are maps of photospheric *brightness* in a narrow subinterval of the visible spectrum. However, in the context of 'cool' stars, like OU And, the CLDI maps can be interpreted as good proxies of temperature maps, though they lack a temperature calibration (see e.g. Wolter+ 2005).

Keeping that in mind, our (proxy) temperature maps of OU And for 2008 and 2013 are in a good agreement with the magnetic maps published in BEAL16, which were taken strictly contemporaneously. Our temperature maps confirm the reality of a persistent and large polar spot on OU And, as already found by BEAL16. Furthermore, like the magnetic maps, our temperature maps show smaller cool spots closer to the equator. Unfortu-

nately, as discussed in detail in Sect. 3.4, we cannot trace the evolution and precise location of these spots on the basis of our dataset.

Our study of the activity indices consists of 'snapshots' taken between 2008 and 2017, each snapshot covering at most a few stellar rotations contiguously. In agreement with BEAL16, for all our observations, we found only modest variations in chromospheric activity, e.g. with an amplitude of a few percent peak-to-peak in terms of the S-index. During our study, OU And showed the most pronounced chromospheric variations in 2013; this holds true for all activity indices and the corresponding chromospheric emission *line profiles*.

As already discussed by BEAL16, we presume that OU And is an Ap star descendant that has evolved close to the end of the Hertzsprung gap, still retaining a relatively fast rotation from its main sequence phase. Together with the expected remnant strong magnetic field from its Ap star past, this fast rotation results in an efficient dynamo operation, see also BEAL16.

We note that BEAL16's magnetic map for 2013 showed a decrease of the poloidal component of the magnetic field, when compared to the 2008 maps. This decrease was accompanied by an increase of the toroidal field. Together with the long-term chromospheric variations found in our study, this could indicate a weak cycle of OU And's magnetic activity. Similar long-term variations have recently been found for the K giant OP And (Georgiev et al. 2019).

While we find weak long-term variations of OU And's chromospheric emission, these variations neither suggest rotational modulation nor a cyclic behaviour in the framework of our analysis. As in the case of other tentative activity cycle candidates, further extensive spectroscopic long-term studies of OU And will be required to support or refute the reality of such a cycle.

6 Acknowledgements

UW acknowledges funding by DLR, project 50OR1701; AB and RK-A acknowledge financial support in the framework of DNTS Germania 01/10. We make use of data obtained with the NARVAL spectrograph (OPTICON programs for semesters 2008B and 2015A). NARVAL observations obtained in 2013 were funded by project BG051PO001-3.3.06-0047 and financed by the EU, ESF and Republic of Bulgaria.

Based on observations taken with the TIGRE telescope, located at La Luz, Mexico. TIGRE is a joint collaboration of the Hamburger Sternwarte, the University of Guanajuato and the University of Liège.

The leading author of this article died unexpectedly in November 2017. Ana initiated this study and we have completed it along the lines set out by her and Uwe several years ago. We mourn the loss of an esteemed colleague and a great person. May Ana rest in peace.

References

Ayres T. R., Hodges-Kluck E., Brown A., 2007, *ApJS*, 171,304

- Barnes J. R., Collier Cameron A., James D. J., Donati, J.-F., 2000, *MNRAS*, 314, 162
 Borisova A., Aurière M., Petit P., Konstantinova-Antova R., Charbonnel C., Drake N. A., 2016, *A&A*, 591A, 57B
 Bruls J. H. M. J., Solaki S. K., Schüssler M., 1998, *A&A*, 336, 231
 Cowley A. P., Bidelman, W. P., 1979, *PASP*, 91, 83
 de Medeiros J. R., Mayor M., 1999, *A&AS*, 139, 433
 Deutsch A. J., 1954, *IAU Symp.* 6, 209
 Donati J.-F., Catala C., Landstreet J. D., and Petit, P., 2006, *ASPC*, 358, 362
 Donati J.-F., Semel M., Carter B.D., Rees D.E., Collier Cameron A., 1997, *MNRAS*, 291
 ESA, 1997, *VizieR Online Data Catalog*, 1239,0
 Glebocki R., Gnacinski P., Stawikowski A., 2000, *AcA*, 50, 209
 Gondoin P., 1999, *A&A*, 352, 217
 Gondoin P., 2003, *A&A*, 409, 263
 S. Georgiev, R. Konstantinova-Antova, A. Borisova, D. Kolev, M. Auriere, P. Petit, et al., 2019, *AIP Conference Proceedings* 2075, 090003
 Gray R. O., Graham P. W., Hoyt, S. R., 2001, *AJ*, 121, 2159
 Gray R. O., Napier M. G., Winkler L. I., 2001, *AJ*, 121, 2148
 Högbom J. A., 1974, *A&AS*, 15, 417
 Hopkins J. L., Boyd L. J., Genet R. M., Hall D. S., 1985 *IBVS*, 2684, 1
 Husser T.-O., Wende-von Berg S., Dreizler S., Homeier D., Reiners A., Barman T., Hauschildt, P. H., 2013, *A&A*, 553, 6
 Khochukhov O., Piskunov N. E., 2002, *A&A* 381, 736
 Khochukhov O., Drake N. A., Piskunov N. E., 2004, *A&A* 424, 935
 Kővari Z., Olah K., Kriskovics L., et al., 2017, *AN* 338, 903
 Kurucz R., 1993, *SYNTHE Spectrum Synthesis Programs and Line Data. Kurucz CD-ROM No. 18. Cambridge, Mass.: Smithsonian Astrophysical Observatory, 1993.*
 Mittag M., Schröder K.-P., Hempelmann A., Gonzalez-Perez J. N., Schmitt J. H. M. M., 2016, *A&A*, 591, 89
 Mittag M., Hempelmann A., Schmitt J. H. M. M., Fuhrmeister B., Gonzalez-Perez J. N., Schröder K.-P., 2017, *A&A*, 607, 87
 Mittag M., Hempelmann A., Fuhrmeister B., Czesla S., Schmitt J.H.M.M., 2018, *AN*, 339
 Piskunov N. E., Valenti J., 2002, *A&A*, 385, 1095
 Strassmeier K. G., Hall D. S., 1988, *ApJS*, 67, 453
 Strassmeier K. G., Serkowsch E., Granzer Th., 1999, *A&AS*, 140, 29
 Strassmeier K. G., 2009, *A&A Rv*, 17, 251
 van Leeuwen F., 2007, *A&A*, 474, 653
 Wolter U., Schmitt J. H. M. M., van Wyk F., 2005, *A&A*, 435, 261
 Wolter U., Robrade J., Schmitt J. H. M. M., Ness J.-U., 2008, *A&A Lett.*, 478, 11